IEEE Access
Multidisciplinary | Rapid Review | Open Access Journal

Received January 6, 2020, accepted January 25, 2020, date of publication January 30, 2020, date of current version February 6, 2020.

Digital Object Identifier 10.1109/ACCESS.2020.2970544

An Accurate Method for Designing, Characterizing, and Testing a Multi-Layer Radome for mm-Wave Applications

ZEESHAN QAMAR, (Member, IEEE), NAFATI ABOSERWAL, (Member, IEEE), AND JORGE L. SALAZAR-CERRENO, (Senior Member, IEEE)
School of Electrical and Computer Engineering, The University of Oklahoma, Norman, OK 73019, USA
Advanced Radar Research Center (ARRC), The University of Oklahoma, Norman, OK 73019, USA

Corresponding author: Jorge L. Salazar-Cerreno (salazar@ou.edu)

ABSTRACT This paper presents an accurate procedure to design, characterize and test a radome for millimeter-wave applications. In this procedure, an accurate analytical model is presented to design a radome structure that takes into consideration the bandwidth, losses, reflections and depolarization factor as a function of frequency and incident angle. To guarantee a good operational electrical performance, the proposed procedure includes a material characterization and accurate test procedure based on the free-space Gaussian beam method and time gating filtering technique. Four radomes (two-monolithic and two A-sandwich) at 82 GHz and 94 GHz are designed, characterized and tested to validate the proposed technique. Results obtained with this procedure are compared with numerical simulations and experimental results. This method is shown to be accurate and versatile for radomes in mm-Wave applications.

INDEX TERMS A-sandwich, mm-Wave, monolithic, multi-layer, radome, W-band.

I. INTRODUCTION

Radomeis an essential part of radar or communications systems where its main task is to protect a system against wind, rain, pollution and other environmental elements with a structure that is electromagnetically transparent for the system. Electromagnetic transparency consists of low-reflection, low-insertion loss, and minimum distortion of signal polarization [1]. The radome also provides mechanical strength to protect the antenna from wind loading and provides stability and integrity for mitigating environmental conditions such as temperature, humidity and pressure. Also, the radome reduces the operation and maintenance cost of the system and increases its life span [1], [2].

Radio frequencies (RF) available for radar and satellite communication systems have been expanded into millimeter-wave (mm-Wave), specifically W-band, to accommodate the increased bandwidth requirements. Impressive data rate throughput capacity that W-band offers is another important feature that attracts various communication technologies. For instance, International Telecommunication Union (ITU) the main regulatory agency in this area, allocated frequency segments of 71 GHz to 76 GHz for transmitting and 81 GHz to 86 GHz for receiving in satellite services [3]. A frequency band from 76 GHz to 81 GHz is also used in cruise control radars for autonomous car systems [4]. The atmospheric radio window for imaging millimeter-wave radar applications in astronomy, defense, and security applications is used at 94 GHz [3], [5], [6]. All major commercial radar and satellite operators show high interest toward allocations of W-band slots for radar and satellite communication, obviously planning to implement their commercial projects in W-band in the near future [7].

Several radome configurations are used to minimize RF reflections, including half-wave, A-sandwich, double A-sandwiches, and multiple A-sandwiches, as shown in Fig. 1a [8]. The best-suited configuration for a particular application depends on the mechanical requirements of radome and its operating frequency. Monolithic (half-wave) can provide the best uniformity, but usually, it is only applicable when radome and antenna are fixed together as otherwise, the incident angle can vary dramatically during antenna scanning and cause highly unstable EM performance degradation. Whereas multi-layer radome provides more bandwidth and a

The associate editor coordinating the review of this manuscript and approving it for publication was Abhishek Kandwal.

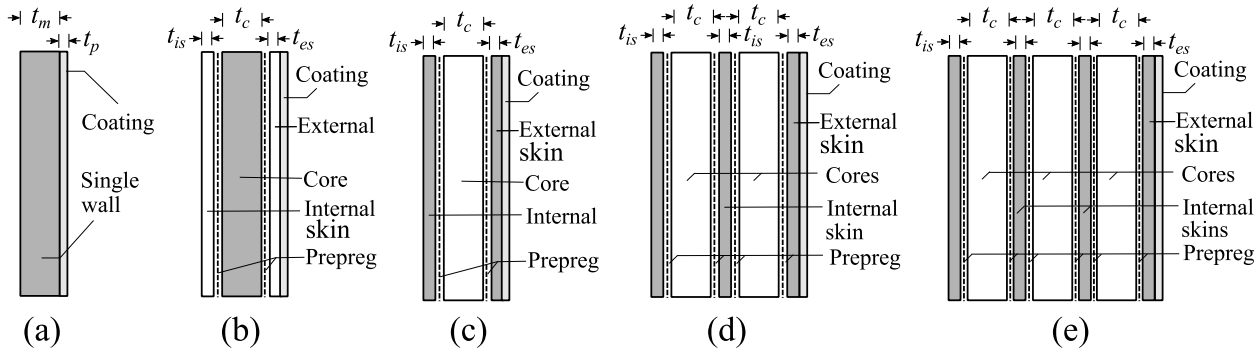

FIGURE 1. Types of Radomes; (a) Monolithic, (b) B-sandwich, (c) A-sandwich, (d) Double A-sandwich, and (e) Multiple A-sandwich.

large scanning range. Another advantage of the multi-layer radome is its high strength-to-weight ratio required by some applications, such as spacecraft. A-sandwich is typically used multi-layer radome in most applications. It consists of three layers: two high-density skins and low-density core material. The permittivity of the skins is greater than the core permittivity. The duality of A-sandwich is called B-sandwich (Fig. 1b), in which the permittivity of the skins is lower than the core permittivity. Double A-sandwich radome, also called C-sandwich (Fig. 1d), has five layers and enables the residual reflections from individual A-sandwiches to be further canceled. A typical double A-sandwich radome consist of two core layers (foam or honeycomb) separated by a central skin layer along with two skin layers on the outside of each core-forming interior and exterior of the radome. Radome wall having more than two A-sandwich is called a multiple A-sandwich radome (Fig. 1e). The electrical characteristics of any type of radome depend on three parameters. The first one is thickness, second is permittivity, and the third is the angle of incidence. The overall transmission characteristics of radome are further affected by the polarization angle which is determined by the radome normal, incident direction, and polarization of the electromagnetic (EM) wave.

Different types of radomes and their impact over a radar and communication system have been reported [2], [9]–[17]. Some of them for high frequencies and others for low frequencies i.e. C-band, X-band, etc. However, very little work has been reported for radomes in high frequencies, especially for W-band. The mitigation of the wet antenna effect from the reflector dish antenna at 72 GHz and 84 GHz has been reported in [2]. An automotive radome has been designed using an anti-reflection surface from 76 GHz to 81 GHz [18], [19].

In this paper, an accurate procedure to design, characterize and test a radome for W-band applications is presented. An analytical model to perform the design trade-off of a radome that takes into consideration the bandwidth, losses, reflections, and polarization as a function of incident angle is utilized. Moreover, the dependence of permittivity on temperature for radome materials is also discussed. To support the development of good performance radomes, the proposed procedure includes a material characterization having an accurate test procedure based on the free-space Gaussian beam method and time gating filtering technique. To validate the proposed method, four radomes (two-monolithic and two A-sandwich) at 82 GHz and 94 GHz were designed, characterized and tested. Good agreements are obtained between calculated, simulated and measured results.

II. THEORY

The expressions (1) and (2) can be used to compute the dimensions of monolithic and multi-layer radomes, respectively [8], [14]. These expressions require the condition of zero transmission loss. In other words, all the layers computed using these expressions should be lossless. However, the transmission line model has subsequently been discussed considering the lossy materials for radome design. Moreover, these expressions also provide the radome dimensions at an oblique angle. For the monolithic radome wall (Fig. 1a), the material's thickness (t_m) relative to its permittivity (ε_r) is an integral multiple of half-wavelength.

$$t_m = \frac{N\lambda_o}{2\sqrt{\varepsilon_r - sin^2(\theta_i)}} \tag{1}$$

where θ_i is the angle of incidence, λ_o is the free space wavelength and $N = 1, 2, 3, \ldots$ is the number of order.

In the case of multi-layer radome (A-, B- and C-sandwich), the thickness can be varied by modifying the thickness of the core layers concerning its permittivity and skin parameters (thickness and permittivity) using (2).

$$t_c = \frac{\lambda_o}{2\pi\sqrt{\varepsilon_c - sin^2(\theta_i)}}\left[N\pi - tan^{-1}\left(\frac{Num}{Den}\right)\right] \tag{2}$$

$$Num = 2(\varepsilon_s - 1)\sqrt{\varepsilon_s\varepsilon_c}\, sin(2\phi_s) \tag{3}$$

$$Den = (\varepsilon_s+1)(\varepsilon_c-\varepsilon_s)+(\varepsilon_s-1)(\varepsilon_s+\varepsilon_c)\, cos(2\phi_s) \tag{4}$$

$$\phi_s = \frac{2\pi\ t_s}{\lambda_0}\sqrt{\varepsilon_s - sin^2(\theta_i)} \tag{5}$$

where t_s is the skin thickness, t_c is the core thickness, ε_s is the skin permittivity and ε_c is the core permittivity. To laminate a multi-layer radome prepreg or bond ply is required to combine different materials (skin and core) to design any multi-layer radome. Moreover, the exterior skin layer of the radome also requires coating/paint to safe the radome from

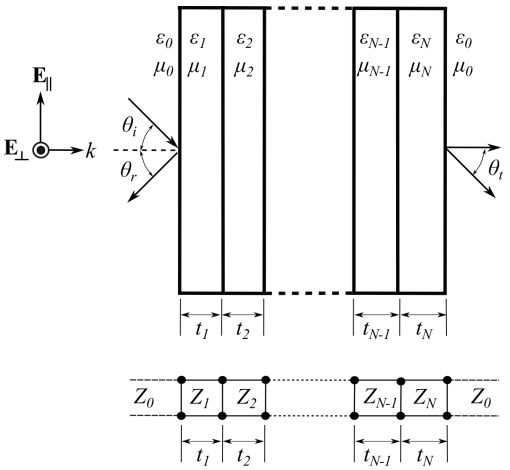

FIGURE 2. Representation of a planar multi-layer radome using the equivalent transmission line model.

environmental hazards. The permittivity and thickness of these prepreg/bond ply and coating slightly affect the EM performance of radome such as a shift in the resonant frequency. For ease of radome designing, bond ply and coating are previously being ignored due to the small thickness of these materials. However, there will be a significant effect at mm-Wave range. Therefore, the effective permittivity (ε_{eff}) of the skin and bond ply/coating can be calculated using (6), which can be used in (2) to obtain the core dimensions for multi-layer radome design.

$$\varepsilon_{eff} = \sum_{n=1}^{N} \varepsilon_n \left(\frac{t_n}{t_1 + t_2 + \ldots + t_N} \right) \tag{6}$$

where ε_n and t_n are the permittivity and thickness of each material, respectively.

A. TRANSMISSION LINE MODEL

The equivalent transmission line model has also been implemented to extract the frequency response of different types of radomes, as shown in Fig. 2 [20]. Using this model, single homogeneous material for monolithic radome or multiple layers of different electrical parameters and thicknesses can be combined to form any type of multi-layer radome shown in Fig. 1. This model can use lossy dielectrics, therefore, they are fully characterized by ε and tanδ, whereas the permeability $\mu = 1$ is considered. The field analysis can be seen in Fig. 2. Equations (7)-(17) are used to calculate the overall reflection and transmission coefficients of proposed radome for perpendicular and parallel polarizations.

$$\Gamma_\perp = \frac{B_0}{A_0}, \quad T_\perp = \frac{1}{A_0} \tag{7}$$

$$\Gamma_\parallel = \frac{D_0}{C_0}, \quad T_\parallel = \frac{1}{C_0} \tag{8}$$

The A_0, B_0, C_0 and D_0 are found using the recursive formulas

$$A_n = \frac{e^{+\psi_n}}{2}[A_{n+1}(1 + Y_{n+1}) + B_{n+1}(1 - Y_{n+1})] \tag{9}$$

$$B_n = \frac{e^{-\psi_n}}{2}[A_{n+1}(1 - Y_{n+1}) + B_{n+1}(1 + Y_{n+1})] \tag{10}$$

$$C_n = \frac{e^{+\psi_n}}{2}[C_{n+1}(1 + Z_{n+1}) + D_{n+1}(1 - Z_{n+1})] \tag{11}$$

$$D_n = \frac{e^{-\psi_n}}{2}[C_{n+1}(1 - Z_{n+1}) + D_{n+1}(1 + Z_{n+1})] \tag{12}$$

where

$$A_{N+1} = C_{N+1} = 1, \quad B_{N+1} = D_{N+1} = 0 \tag{13}$$

$$Y_{n+1} = \frac{cos\theta_{n+1}}{cos\theta_n} \sqrt{\frac{\varepsilon_{n+1}(1 - jtan\delta_{n+1})\mu_n}{\varepsilon_n(1 - jtan\delta_n)\mu_{n+1}}} \tag{14}$$

$$Z_{n+1} = \frac{cos\theta_{n+1}}{cos\theta_n} \sqrt{\frac{\varepsilon_n(1 - jtan\delta_n)\mu_{n+1}}{\varepsilon_{n+1}(1 - jtan\delta_{n+1})\mu_n}} \tag{15}$$

$$\psi_n = t_n \gamma_n cos\theta_n \tag{16}$$

$$\gamma_n = \sqrt{j\omega\mu_n(\sigma_n + j\omega\varepsilon_n)} = j\omega\sqrt{\mu_n\varepsilon_n(1 - jtan\delta_n)} \tag{17}$$

where $n = 0, 1, 2, 3, \ldots, N$, where N is the number of layers, t_n is the thickness of each layer and θ_n is the complex angle of refraction in the n^{th} layer.

B. TEMPERATURE EFFECT ON MATERIALS

Many useful materials for designing radomes have limited resistance to heat, whereas some materials that are tough at moderate temperatures become extremely brittle at low temperatures. The selection of materials is very critical as high/low temperatures may rule out many materials that are even satisfactory. Even some materials, survive at extreme temperatures, have a notable change in their electrical properties such as the permittivity of the material. Material tolerance on this parameter, especially for mm-Wave range at high/low temperature, is sometimes insufficient. Therefore, the change in permittivity at different temperatures should be known in order to predict the frequency response of the radome. The change in permittivity at different temperatures can be calculated using the expression (18) [21].

$$\frac{\delta\varepsilon_r}{\varepsilon_r} = 2\alpha_t \delta T \tag{18}$$

where $\delta\varepsilon_r$ is the change in relative permittivity, δT is the change in temperature and α_t is the thermal coefficient expansion (TCE) in ppm/°C.

C. DEPOLARIZATION EFFECT

There are two main polarization components (perpendicular and parallel) of plane wave incident onto the radome's wall. The transmission difference of these two components can induce a cross-polarization. When radome depolarization is high, it deteriorates the cross-polarization performance of the radar or communication system. This adverse effect is critical for a polarimetric radar system that requires high isolation (>40 dB) between polarization channels [17]. The intensity of the depolarization ratio depends on the amplitude and phase of the complex transmission coefficients. And these coefficients depend upon the incident angle and

TABLE 1. Radome materials [21]–[23].

	Material	ε (W-band)	Tanδ (W-band)	TCE (Boresight) (ppm/ °C)
Core	RohaCell 51HF	1.048	0.0135	33.4
	Nomex	1.10	0.0030	-
	Divinyll cell HP	1.07	0.0030	40.0
	Polyurethane FR3703	1.04	0.0017	35.0
Skin	RO5880	2.19	0.0013	237
	PTFE Gortex	2.00	0.0002	-
	Fiber Glass-E	6.30	0.0037	5.00
	Fiber Glass-S	6.00	0.0020	2.90
	Fiber Glass-D	4.60	0.0015	3.00
	Kevlar 49	3.70	0.0020	-5.00
	Quartz	3.60	0.0120	0.55
Prepreg/bond ply	3M Adhesive	2.35	0.0250	5.84
	E-glass Epoxy	4.20	0.0160	6.30
	D-glass Epoxy	3.45	0.0090	8.90
	Spectra epoxy	2.80	0.0040	6.40
	Quartz epoxy	3.20	0.0110	7.20
Paint/coating	Hirec100	4.47	0.0139	-
	Cytonix	3.00	0.0200	-
	Esscolam10	3.00	0.0090	-

the tilt of the plane of polarization. All these parameters must be determined and taken into account at the appropriate stage. For purely parallel or perpendicular incidence the cross-polarization vanishes, as in each case, one of the resolved components is zero. This polarization factor of any radome type can be calculated using 19 [1].

$$DP_R = \sqrt{\frac{1 - 2kcos(\phi_{\parallel} - \phi_{\perp}) + k^2}{cot^2\theta_i + 2kcos(\phi_{\parallel} - \phi_{\perp}) + k^2 tan^2\theta_i}} \quad (19)$$

where $k = |T_{\perp}| / |T_{\parallel}|$ and $(\phi_{\parallel} - \phi_{\perp})$ is the phase difference of respective polarizations and θ_i is the angle of incidence. The depolarization effect was evaluated for different radomes and the results are discussed in the following section.

III. MATERIALS FOR RADOME

Currently, many materials are used to design radomes having permittivity ranging from 1 to 10 and tangent-loss from 0.0003 to 0.011 in the W-band range. Comparative data on these materials are shown in Table 1 [21]–[23]. For monolithic and A-sandwich's skin layers, Rogers-5880 has been used. This material has dimensional stability, relatively low electrical losses at high frequencies (tanδ = 0.0009) and good copper adhesion. As systems move to higher frequencies, other substrate materials have high losses and quite expensive compared to Rogers-5880 [24].

In the case of core material in A-sandwich radome, Rohacell-51HF is widely used. This material has a smaller cell structure that takes up less resin. At any rate, the mechanical and thermal properties of Rohacell remain unchanged. This material is used as a structural core in connection with vacuum infusion processes. The cell size of this material represents an optimal compromise between low resin uptake and better bonding of the facings to the foam core [25].

For prepreg/bond ply, 3M adhesive transfer tape has been used. This material has a high-temperature acrylic adhesive, which can be exposed to 232°C. This material has exceptional perfect values even at extreme temperatures. This material also has low out-gassing properties, which is an important consideration for the automotive, aerospace and electronics industries [26]. Moreover, this material has a high bonding strength that allows a strong connection between the skin and core layers.

IV. DESIGN, FABRICATION, AND MEASUREMENTS

For the radome design, firstly chosen materials are characterized over the entire W-band range from 75 GHz to 110 GHz. Then, four different types of radomes (Fig. 8) are designed, simulated in commercially available Ansoft HFSS and measured. Three radomes (two monolithic and one A-sandwich) are designed for 82 GHz at a boresight incident angle. These radomes can be used in satellite communication systems that cover a frequency range from 81 GHz to 86 GHz. The thickness of monolithic radomes is considered in such a way that they provide good results at 45° tilted angle for 94 GHz frequency band. Then another A-sandwich radome is designed for the same 94 GHz band tilted at 45°. These radomes can be used in imaging mm-Wave radar and defense applications. The dimensions of the proposed radomes are shown in Table 2. For monolithic radomes, different thickness of the material is not easily available, therefore material (Rogers-5880) of different thicknesses are laminated together

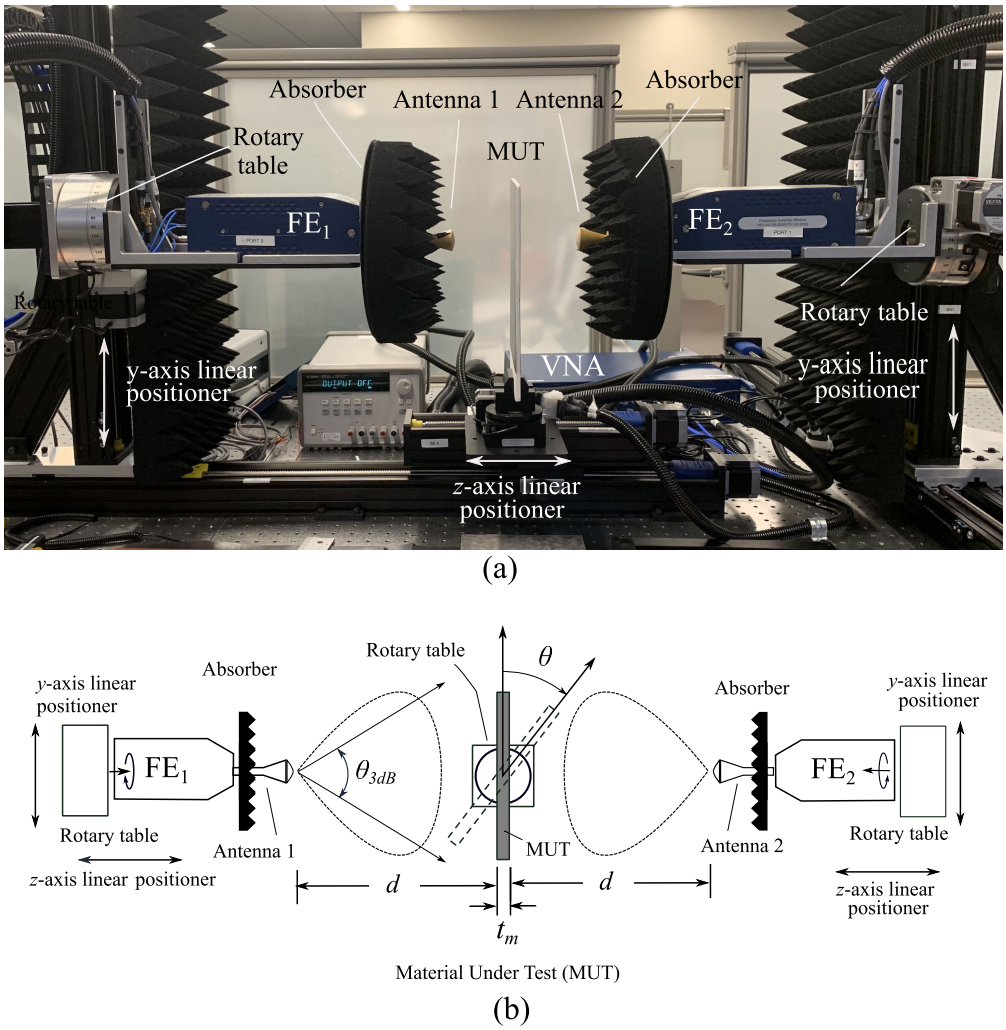

FIGURE 3. Material under test setup. (a) Picture of the 9-axis mm-Wave RF scanner measurement setup for the characterization of proposed radomes and (b) Graphical representation of the top view of the MUT setup for testing a material over incident angle θ.

using a compatible prepreg/bond ply to obtain the desired thickness, making it a quasi-monolithic radome. The physical and electrical dimensions of prepreg are also considered in the modeling and designing process to obtain accurate results.

A. MEASUREMENT SETUP

As shown in Fig. 3a, 9-axis mm-Wave scanner is used for the characterization of materials and radomes. This state to the art system has a position accuracy up to 35 μm. A vector network analyzer (Copper Mountain C4209) is connected with two frequency extenders (FE), which cover the entire W-band. Linear positioners are used to align ($x-$, $y-$ and $z-$ axis) the frequency extenders, antennas, and MUT. Two lenses corrected conical horn antennas operating at W-band are used for this setup. This antenna has a gain of 26 dBi with a 3 dB beam-width of 7° and 9° in the E- and H-plane, respectively. Unlike spot focusing antennas, this lens corrected antenna generates plane wavefront at a very short distance of the antenna, which allows characterizing the materials and radomes at a very short distance. However, the size of the material under test (MUT) and 3 dB beamwidth (θ_{3dB}) of the antenna in the E-and H-plane restricts the distance between the antenna and the MUT as shown in Fig. 3b.

This system can measure the transmission and reflection coefficient at boresight, whereas only the transmission coefficient at oblique incident angles. Free space thru, reflect and delay line (TRL) measurement technique is used to characterize materials and/or radomes at boresight. This free-space calibration method is contact-less and able to accommodate large and flat sheets of materials [27], [28]. To measure the materials/radomes at oblique incident angles, the thru response (TR) calibration technique is used. Finally, after each calibration method, time gating technique is implemented to eliminate the effects of the reflections from the system [29]–[31].

B. MATERIAL CHARACTERIZATION AND TEMPERATURE EFFECT

Fig. 4 shows the measured and simulated permittivity and tangent-loss of Rogers-5880 and Rohacell-51HF.

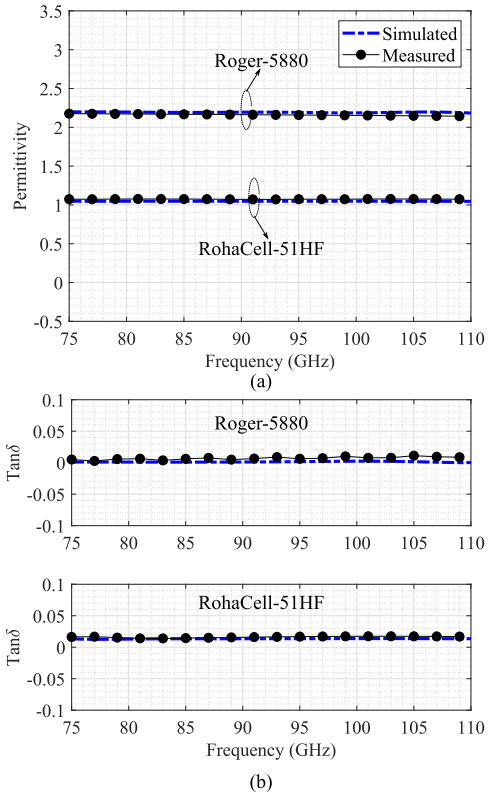

FIGURE 4. Simulated and measured constitutive electrical parameters of radome's materials. (a) Permittivity. (b) Tangent loss.

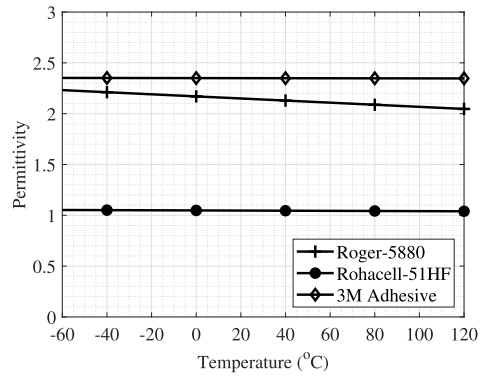

FIGURE 5. Dependence of dielectric constant on temperature for radome's core and skin.

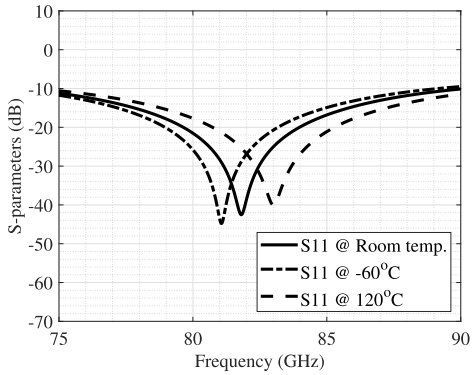

FIGURE 6. Simulated *S*-parameters of 3rd order monolithic radome at different temperatures.

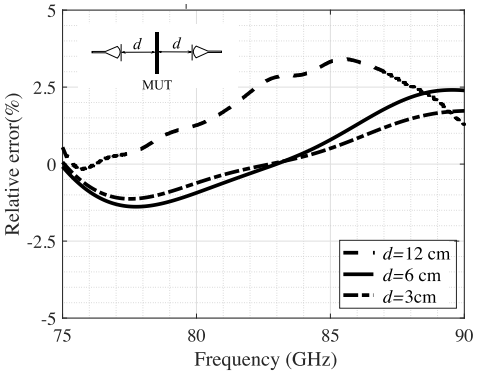

FIGURE 7. Measurement of relative errors for 3^{r} *d* order A-sandwich radome for different distances (d = 12 cm, d = 6 cm, and d = 3 cm) between antennas and material under test.

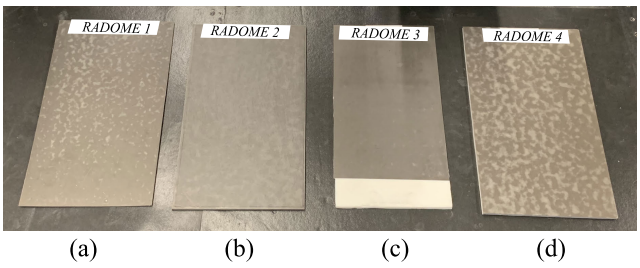

FIGURE 8. Picture of radomes under test. (a) Monolithic 1st order (Radome 1), (b) Monolithic 3st order (Radome 2), (c) A-sandwich 3rd order (Radome 3) and (d) A-sandwich 2nd order (Radome 4).

The measured permittivity is recorded 2.16 and tangent loss 0.002-0.006 for the entire W-band band from 75 GHz to 110 GHz. For Rohacell-51HF, the permittivity equals to 1.05 and tangent loss ranges from 0.013 to 0.016 are recorded.

As previously mentioned, the permittivity of the material changes as the temperature changes. Therefore, the change in permittivity at a different temperature should be known to predict the frequency response of the radome. The temperature-dependent permittivities of all the chosen materials are calculated using (18) and shown in Fig. 5. The core material RohaCell-51HF has permittivity tolerance from 1.042 to 1.054 over a temperature range from −60°C to 120°C. Whereas the skin Rogers-5880 has a permittivity tolerance ranges from 2.048 to 2.232 and the prepreg/bond ply has ranged from 2.347 to 2.352. To estimate the change in frequency, the radomes are simulated with permittivities calculated at −60°C and 120°C temperatures using (18).

Rogers-5880 at extreme temperature is more disperse compared to Rohacell and 3M adhesive, therefore 3rd order half-wave monolithic radomes using Rogers-5880 is simulated in Ansoft HFSS at 82 GHz resonant frequency, as shown in Fig. 6 The simulation clearly shows that the resonant frequency is slightly shifted due to the change in temperature.

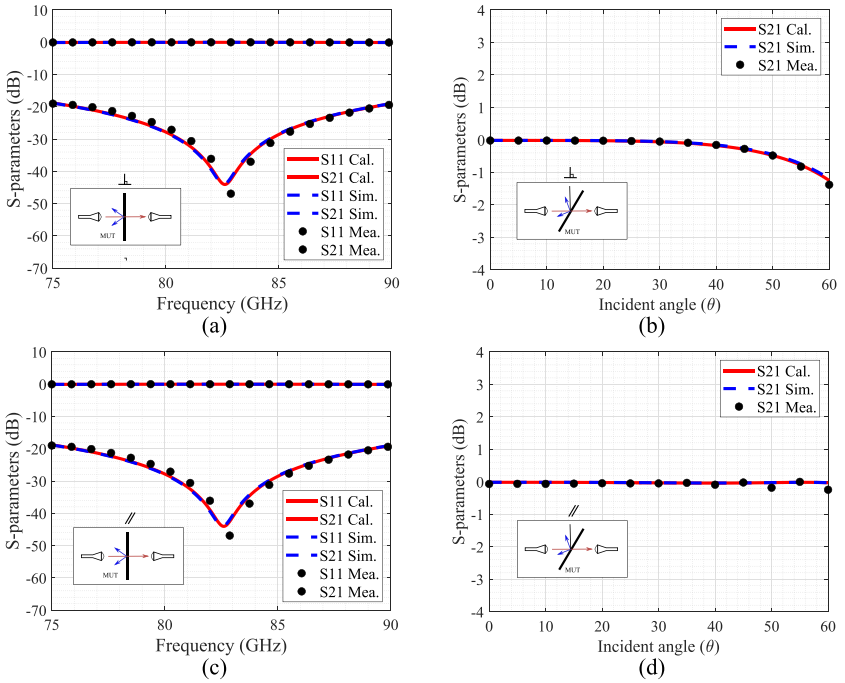

FIGURE 9. Calculated, simulated and measured *S*-parameters of monolithic 1^{st} order radome at 82 GHz. (a) Frequency domain for perpendicular polarization (boresight). (b) Incident angle domain for perpendicular polarization. (c) Frequency domain for parallel polarization (boresight). (d) Incident angle domain for parallel polarization.

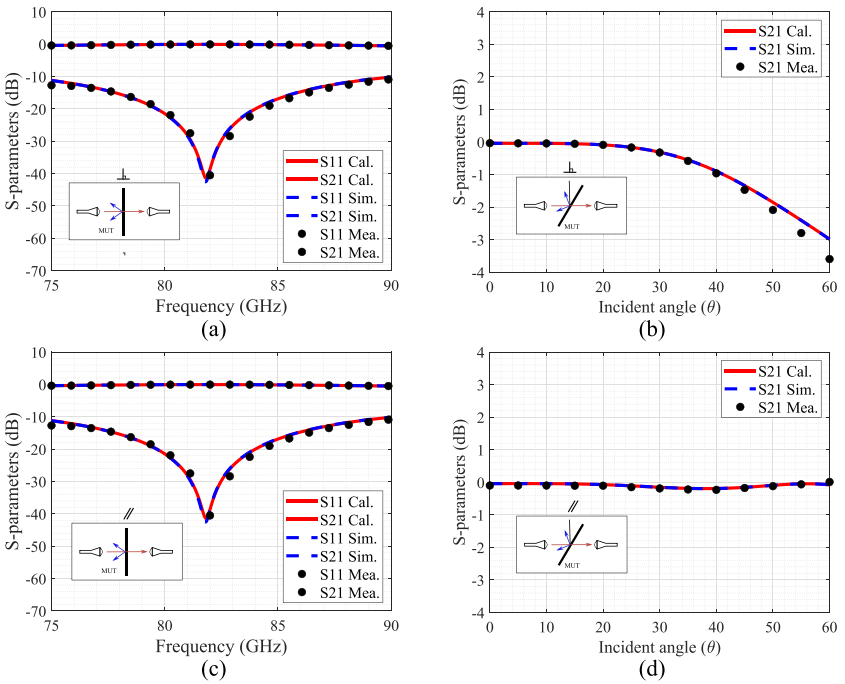

FIGURE 10. Calculated, simulated and measured *S*-parameters of monolithic 3^{rd} order radome at 82 GHz. (a) Frequency domain for perpendicular polarization (boresight). (b) Incident angle domain for perpendicular polarization. (c) Frequency domain for parallel polarization (boresight). (d) Incident angle domain for parallel polarization.

In case of low temperature i.e. −60°C, the frequency-shifted to 81.27 GHz, whereas 83.19 GHz resonant frequency is obtained for high (120°C) temperature. This shows that Over the temperature range from −60°C to 120°C, a maximum change of resonant frequency is 1.45%

C. 82 GHz BORESIGHT RADOMES

As discussed earlier, the distance between the antenna and MUT depends upon the size of the material and the antenna's beam-width. Therefore, 3^{rd} order A-sandwich radomes is measured at boresight considering the different distances for

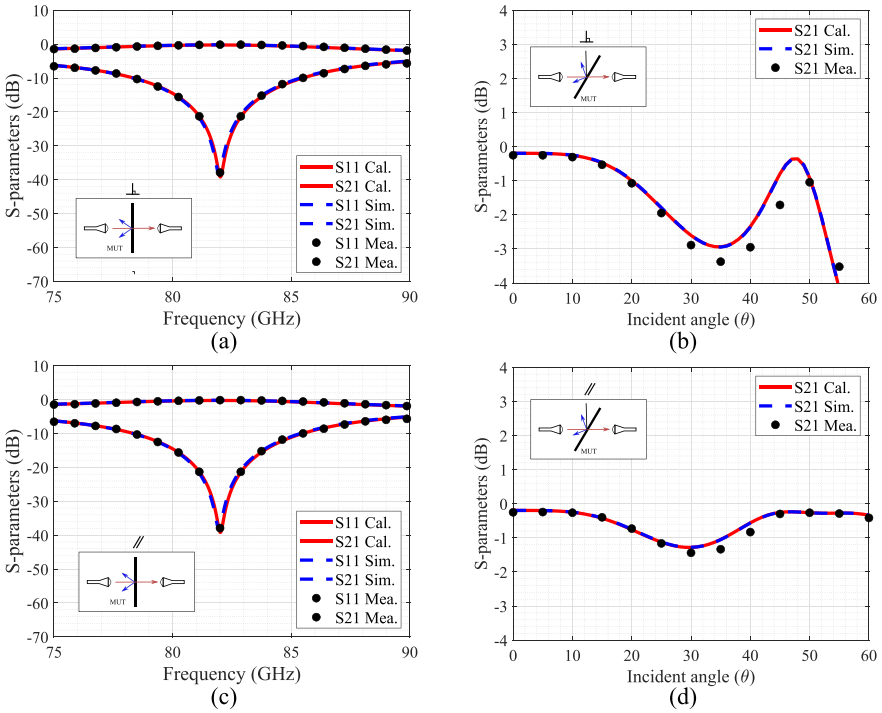

FIGURE 11. Calculated, simulated and measured *S*-parameters of A-sandwich 3rd order radome at 82 GHz. (a) Frequency domain for perpendicular polarization (boresight). (b) Incident angle domain for perpendicular polarization. (c) Frequency domain for parallel polarization (boresight). (b) Incident angle domain for parallel polarization.

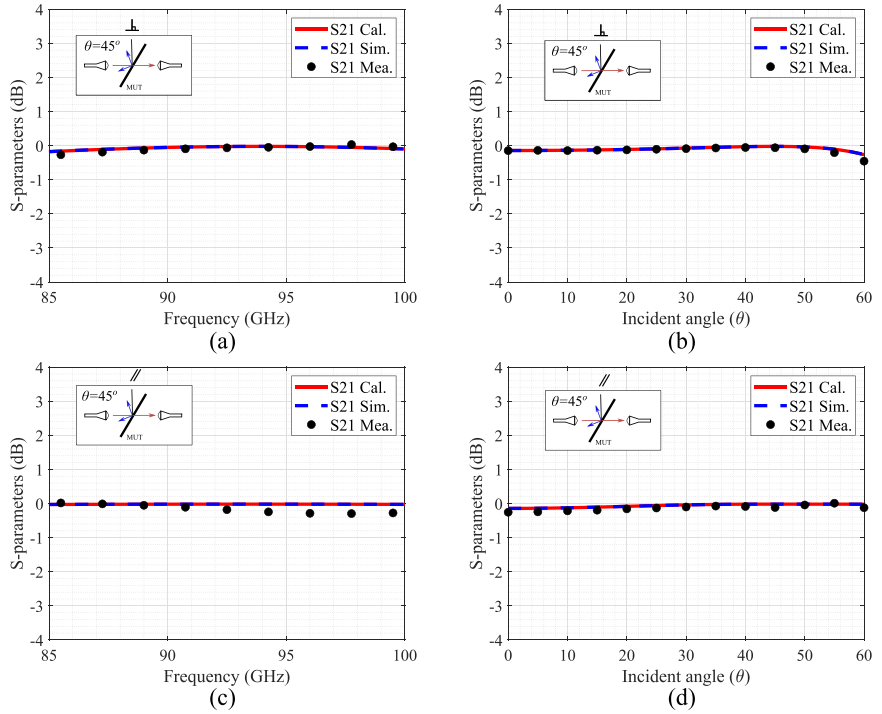

FIGURE 12. Calculated, simulated and measured *S*-parameters of monolithic 1st order radome at 94 GHz. (a) Frequency domain for perpendicular polarization (45°). (b) Incident angle domain for perpendicular polarization. (c) Frequency domain for parallel polarization (45°). (d) Incident angle domain for parallel polarization.

accurate measurements. It can be seen in Fig. 7, the relative error (%) in the measurements with respect to the expected results is 2.63% for a distance of 12 cm. These measurement errors reduce as the distance between the antenna and the

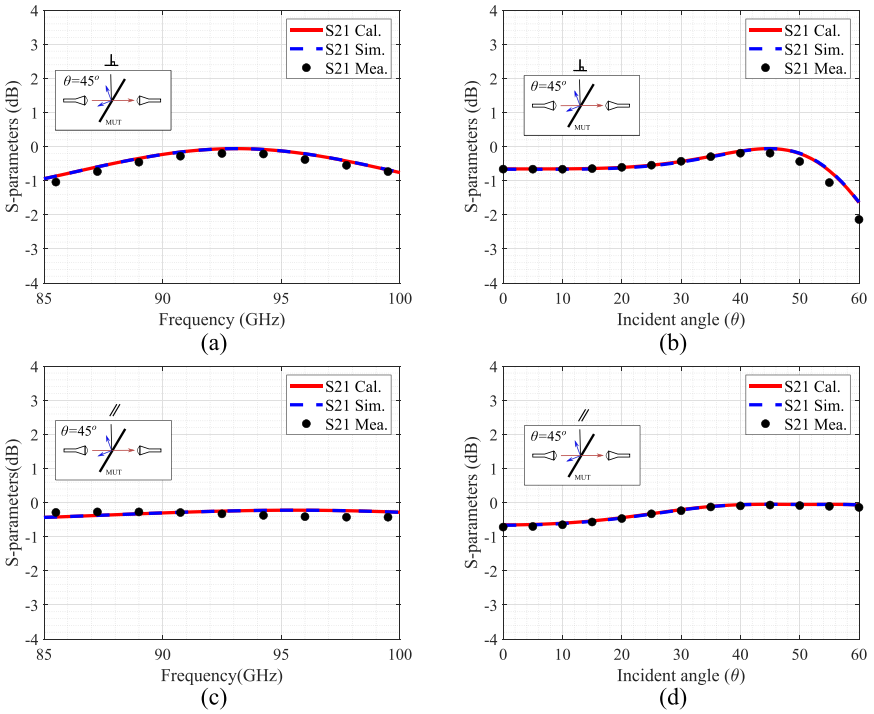

FIGURE 13. Calculated, simulated and measured *S*-parameters of monolithic 3rd order radome at 94 GHz. (a) Frequency domain for perpendicular polarization (45°). (b) Incident angle domain for perpendicular polarization. (c) Frequency domain for parallel polarization (45°). (d) Incident angle domain for parallel polarization.

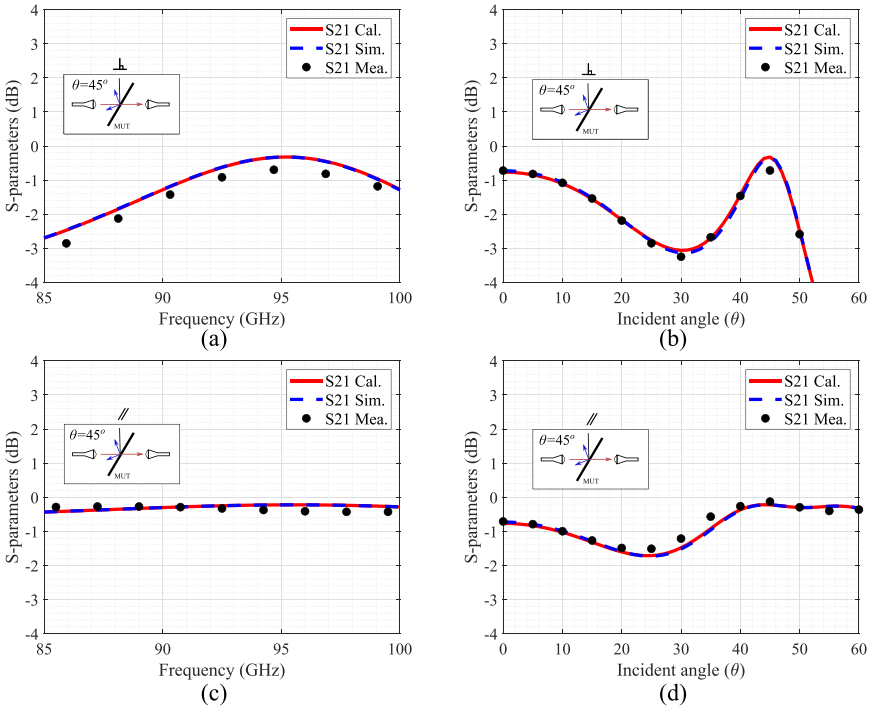

FIGURE 14. Calculated, simulated and measured *S*-parameters of A-sandwich 2nd order radome at 94 GHz. (a) Frequency domain for perpendicular polarization (45°). (b) Incident angle domain for perpendicular polarization. (c) Frequency domain for parallel polarization (45°). (d) Incident angle domain for parallel polarization.

MUT reduces i.e. 2.16% for 6 cm and 1.9% for 3 cm. However, measurements at oblique incident angles are difficult for 3 cm due to the sample size. Therefore, all the radomes are measured with a distance of 6 cm from the antenna.

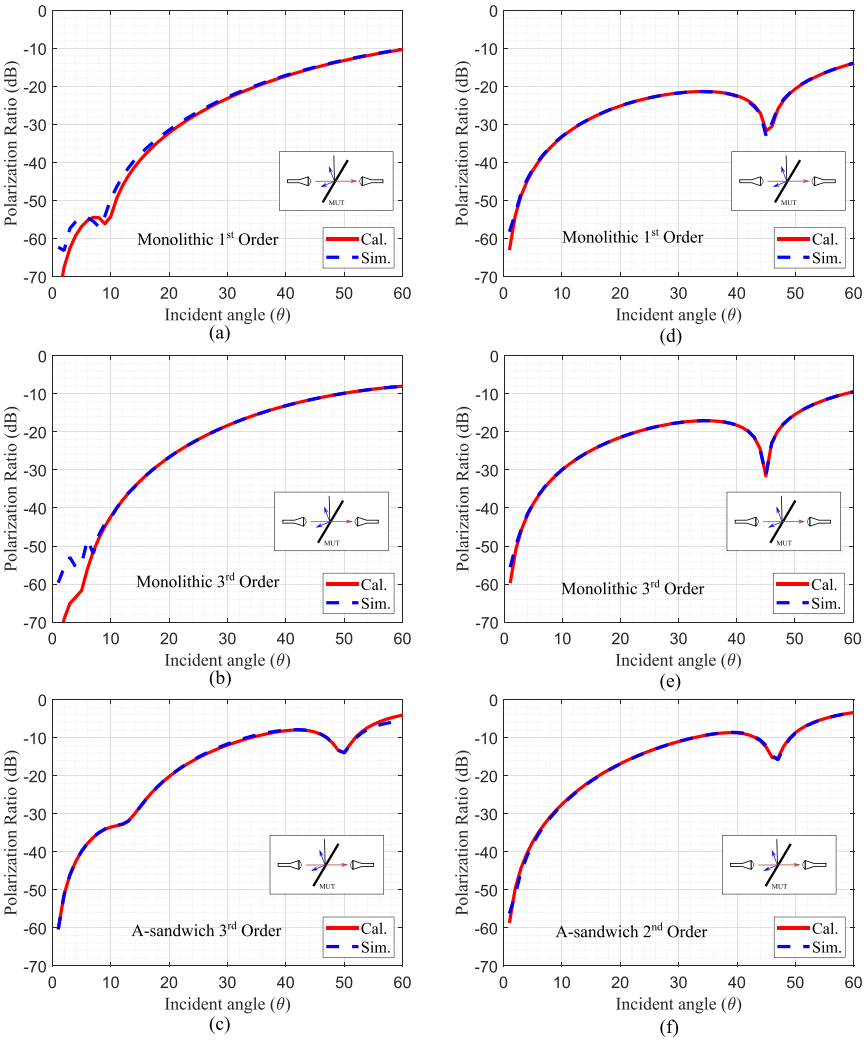

FIGURE 15. Calculated and simulated depolarization ratio of proposed radomes. (a) Monolithic 1^{st} order at 82 GHz (boresight). (b) Monolithic 3^{rd} at 82 GHz (boresight). (c) A-sandwich 3^{rd} order at 82 GHz (boresight). (d) Monolithic 1^{st} order at 94 GHz (45°). (e) Monolithic 3^{rd} at 94 GHz (45°). (f) A-sandwich 2^{nd} order at 94 GHz (45°).

In the 1^{st} order monolithic radome, shown in Fig. 9(a and c) (frequency versus S-parameters), S_{11} less than −20 dB and the worst S_{21} of −0.02 dB are recorded in both perpendicular and parallel polarization for a frequency band from 78 GHz to 87 GHz. The S-parameters as a function of the steering angle for 82 GHz frequency are shown in Fig. 9(b and d). The max relative error of the radome is 0.3% in the frequency domain and 0.6% in the incident angle domain up to 60°.

In the 3^{rd} order monolithic radome, shown in Fig. 10(a and c) (frequency versus S-parameters), S_{11} less than −20 dB and the worst S_{21} of −0.08 dB are recorded in both perpendicular and parallel polarization for a frequency band from 80 GHz to 84 GHz. The S-parameters as a function of the steering angle are shown in Fig. 10(b and d). The max relative error of the radome is 0.35% in the frequency domain and 0.75% in the incident angle domain up to 60°.

In the 3^{rd} order A-sandwich radome, shown in Fig. 11(a and c) (frequency versus S-parameters), S_{11} less than −20 dB and the worst S_{21} of −0.2 dB are recorded in both perpendicular and parallel polarization for a frequency band from 81 GHz to 83 GHz. The S-parameters as a function of the steering angle are shown in Fig. 11(b and d). The max relative error of the radome is 1.15% in the frequency domain and 3.4% in the incident angle domain up to 60°.

D. 94 GHz 45° TILTED RADOMES

In this subsection, the performance analysis of two monolithic radomes (previously designed at 84 GHz frequency band having an incident angle at boresight direction) is conducted at 94 GHz frequency having 45° tilted incident angle. This 1^{st} order monolithic radome, as shown in Fig. 12(a and c) (frequency versus S-parameters), the worst S_{21} of −0.05 dB are recorded in both perpendicular and

TABLE 2. Characterized dimensions and electrical properties of materials used for proposed radomes.

Radomes	Type	Frequency (GHz)	Materials	ε_r	tanδ	thickness (mm)
1	Monolithic 1^{st}order	82@ boresight 94@ 45° tilted angle	Rogers-5880	2.16	0.006	1.010
			Cuclad6700	2.30	0.0025	0.076
			Rogers-5880	2.16	0.006	0.134
2	Monoithic 3^{rd} order	82@ boresight 94@ 45^o tilted angle	Rogers-5880	2.16	0.006	3.260
			Cuclad6700	2.30	0.0025	0.076
			Rogers-5880	2.16	0.006	0.380
3	A-sandwich 3^{rd} order	82@ boresight	Rogers-5880	2.16	0.006	0.254
			3M adhesive	2.35	0.025	0.160
			Rohacell-51HF	1.05	0.016	5.650
			3M adhesive	2.35	0.025	0.160
			Rogers-5880	2.16	0.006	0.254
4	A-sandwich 2^{nd}order	94@ 45° tilted angle	Rogers-5880	2.16	0.006	0.254
			3M adhesive	2.35	0.025	0.160
			Rohacell-51HF	1.05	0.016	4.560
			3M adhesive	2.35	0.025	0.160
			Rogers-5880	2.16	0.006	0.254

parallel polarization for a frequency band from 90 GHz to 96 GHz. The *S*-parameters as a function of the steering angle are shown in Fig. 12(b and d). The max relative error of the radome is 3% in the frequency and incident angle domain.

In the 3^{rd} order monolithic radome, shown in Fig. 13(a and c) (frequency versus *S*-parameters), the worst S_{21} of -0.4 dB are recorded in both perpendicular and parallel polarization for a frequency band from 90 GHz to 96 GHz. The *S*-parameters as a function of steering angle are shown in Fig. 13(b and d). The max relative error of the radome is 4% in the frequency and incident angle domain.

In the 2^{nd} order A-sandwich radome, shown in Fig. 14(a and c) (frequency verses *s*-parameters), the worst S_{21} of -0.6 dB are recorded in both perpendicular and parallel polarization for a frequency band from 92 GHz to 96 GHz. The *S*-parameters as a function of steering angle are shown in Fig. 14(b and d). The max relative error of the radome is 5% in the frequency and incident angle domain.

E. DEPOLARIZATION EFFECT ON PROPOSED RADOME

Experimental characterization in the depolarization ratio (DP_R) of a radome is sensitive to phase accuracy measurement, cross-polarization of the antennas, alignment and spacing between MUT and antennas, and size of the MUT. In this setup, the antennas have a cross-polarization of -30 dB and antenna beamwidth of 9°. For the MUT dimensions (26 cm$\times$16 cm), the projected beamwidth in the MUT surface is slightly larger than the MUT dimensions. This limitation prevents accurate measurements of DP_R. This limitation can be solved replacing the antennas with narrow pattern beamwidth. Ideally, the beamwidth projected to the MUT should be half the MUT dimensions. It also helps to minimize edge effects and coupling between antennas. Increasing the size of the MUT is another option, however, it limits the maximum incident angle. Fig. 3b illustrates this limitation. Fig. 7 presents the relative errors are induced in the transmission coefficient measurements for different spacing between antenna and MUT. By reducing the spacing, lower errors can be induced due to the antenna coupling for having large beamwidth or smaller MUT dimensions. Fig. 15 illustrates the depolarization effect of DP_R produced by the four types of radomes. In all cases, the DP_R was calculated using the expression (19) and then overlapped with simulation results in HFSS. For all the cases (a to d), excellent agreements were found. Small discrepancies were found for the Monolithic radome (3^{rd} order) due to numerical simulation errors due to the thickness of the material. One important and practical observation of the results presented, is the monolithic radomes induce less cross-polarization than A-sandwich radomes.

V. CONCLUSION

In this paper, an accurate procedure to design, characterize and test a radome for millimeter-wave applications is presented. An analytical model to perform the design trade-off of a radome that takes into consideration the bandwidth, transmission losses, reflections and depolarization of a multilayer radome as a function of incident angle and frequency is presented. For validation, four different types of radomes (monolithic and A-sandwich radomes) at 82 GHz and 94 GHz were designed, fabricated and tested. For boresight, relative errors below 1.15% in the transmission coefficient versus frequency were obtained between the proposed model, simulated and measured results. Relative errors below 3.4% were obtained for the same radomes when those were evaluated over an incident angle. Errors less than 5% were obtained for a 45° tilted radome over the incident angle. High errors are due to the small sample and antenna beamwidth used in this setup. A trade-off between accuracy and scanning range was discussed. Large scanning range ($>30°$) requires

large spacing between antennas and MUT, and antennas with narrow beamwidths. Taking into consideration the fabrication tolerances are more sensitive at higher frequencies, prior characterization of the material (dimensions and electrical properties) is required to guarantee high performance radome. The proposed procedure is ideal for radomes where applications require low reflections, low transmission/insertion loss and minimum signal polarization distortion. The advantage of having a 9-axis mm-Wave RF scanner with 35 μm position accuracy enables position correction that helps to minimize alignment errors and improves accuracy of material and radome characterization.

ACKNOWLEDGMENT

The authors would like to thank Dr. Ken Cooper from JPL-NASA for partially supported this work. They would like to thank the Advanced Radar Research Center (ARRC) at The University of Oklahoma for providing the facilities needed to perform this research. They would also like to thank all members of Phased Array Antenna Research and Development group (PAARD) for the discussions and positive feed-backs.

REFERENCES

[1] A. W. Rudge, K. Milne, A. D. Olver, and P. Knight, *The Handbook of Antenna Design*. Edison, NJ, USA: IET, 1982.
[2] E. S. Hong, S. Lane, D. Murrell, N. Tarasenko, and C. Christodoulou, "Mitigation of reflector dish wet antenna effect at 72 and 84 GHz," *IEEE Antennas Wireless Propag. Lett.*, vol. 16, pp. 3100–3103, 2017.
[3] F. Series, "Fixed service use and future trends," Tech. Rep., 2015.
[4] J. Hasch, E. Topak, R. Schnabel, T. Zwick, R. Weigel, and C. Waldschmidt, "Millimeter-wave technology for automotive radar sensors in the 77 GHz frequency band," *IEEE Trans. Microw. Theory Techn.*, vol. 60, no. 3, pp. 845–860, Mar. 2012.
[5] Z. Chen, Y. P. Zhang, A. Bisognin, D. Titz, F. Ferrero, and C. Luxey, "A 94-GHz dual-polarized microstrip mesh array antenna in LTCC technology," *IEEE Antennas Wireless Propag. Lett.*, vol. 15, pp. 634–637, 2016.
[6] W. Gerum, P. Malzahn, and K. Schneider, "94-GHz TWT for military radar applications," *IEEE Trans. Electron Devices*, vol. 48, no. 1, pp. 72–73, Jan. 2001.
[7] H. Xin and M. Liang, "3-D-printed microwave and THz devices using polymer jetting techniques," *Proc. IEEE*, vol. 105, no. 4, pp. 737–755, Apr. 2017.
[8] W. M. Cady, M. B. Karelitz, and L. A. Turner, *Radar Scanners and Radomes*, vol. 26. New York, NY, USA: McGraw-Hill, 1948.
[9] W. Xu, B. Duan, P. Li, and Y. Qiu, "Study on the electromagnetic performance of inhomogeneous radomes for airborne applications—Part I: Characteristics of phase distortion and boresight error," *IEEE Trans. Antennas Propag.*, vol. 65, no. 6, pp. 3162–3174, Jun. 2017.
[10] W. Xu, B. Duan, P. Li, and Y. Qiu, "Study on the electromagnetic performance of inhomogeneous radomes for airborne applications—Part II: The overall comparison with variable thickness radomes," *IEEE Trans. Antennas Propag.*, vol. 65, no. 6, pp. 3175–3183, Jun. 2017.
[11] V. Krushna Kanth and S. Raghavan, "EM design and analysis of frequency selective surface based on substrate-integrated waveguide technology for airborne radome application," *IEEE Trans. Microw. Theory Techn.*, vol. 67, no. 5, pp. 1727–1739, May 2019.
[12] S. Narayan, G. Gulati, B. Sangeetha, and R. U. Nair, "Novel metamaterial-element-based FSS for airborne radome applications," *IEEE Trans. Antennas Propag.*, vol. 66, no. 9, pp. 4695–4707, Sep. 2018.
[13] C. Vinisha, P. Mohammed Yazeen, P. Mahima, V. Joy, and R. Nair, "Multi-layered graded porous radome design for dual-band airborne radar applications," *Electron. Lett.*, vol. 53, no. 3, pp. 189–191, Feb. 2017.
[14] W. Xu, B. Y. Duan, P. Li, and Y. Qiu, "A new efficient thickness profile design method for streamlined airborne radomes," *IEEE Trans. Antennas Propag.*, vol. 65, no. 11, pp. 6190–6195, Nov. 2017.
[15] R. U. Nair and R. M. Jha, "Electromagnetic design and performance analysis of airborne radomes: Trends and perspectives [antenna applications corner]," *IEEE Antennas Propag. Mag.*, vol. 56, no. 4, pp. 276–298, Aug. 2014.
[16] J. Díaz, J. L. Salazar, A. Mancini, and J. G. Colom, "Radome design and experimental characterization of scattering and propagation properties for atmospheric radar applications," in *Proc. Amer. Meteorol. Soc.*, 2014, pp. 819–823.
[17] J. L. Salazar-Cerreño, V. Chandrasekar, J. M. Trabal, P. Siquera, R. Medina, E. Knapp, and D. J. Mclaughlin, "A drop size distribution (DSD)-based model for evaluating the performance of wet radomes for dual-polarized radars," *J. Atmos. Ocean. Technol.*, vol. 31, no. 11, pp. 2409–2430, Nov. 2014.
[18] F. Fitzek and R. Rasshofer, "Automotive radome design–reflection reduction of stratified media," *IEEE Antennas Wireless Propag. Lett.*, vol. 8, pp. 1076–1079, 2009.
[19] F. Fitzek, R. H. Rasshofer, and E. M. Biebl, "Comparison of matching layers for automotive radome design," *Adv. Radio Sci.*, vol. 8, pp. 49–54, Oct. 2010.
[20] C. A. Balanis, *Advanced ngineering Electromagnetics*. Hoboken, NJ, USA: Wiley, 1999.
[21] K. Carver and J. Mink, "Microstrip antenna technology," *IEEE Trans. Antennas Propag.*, vol. 29, no. 1, pp. 2–24, Jan. 1981.
[22] T. E. Nowicki, "Microwave Substrates, Present and Future," Tech. Rep., 1980.
[23] J. W. Lamb, "Miscellaneous data on materials for millimetre and submillimetre optics," *Int J. Inf. Milli. Waves*, vol. 17, no. 12, pp. 1997–2034, Dec. 1996.
[24] *Roger-5880*. Accessed: Jul. 3, 2019. [Online]. Available: https://rogerscorp.com/en/advancedconnectivity-solutions,/rt-duroid-laminates/rt-duroid-5880-laminates
[25] *Rohacell-51HF*. Accessed: Jul. 3, 2019. [Online]. Available: https://www.rohacell.com/product/rohacell/en/products-services/rohacell-hf/
[26] *3M-Adhesive*. Accessed: Jul. 3, 2019. [Online]. Available: https://3m.citrination.com/pif/000313?locale=en-US
[27] M. S. Hilario, B. W. Hoff, B. Jawdat, M. T. Lanagan, Z. W. Cohick, F. W. Dynys, J. A. Mackey, and J. M. Gaone, "*W*-band complex permittivity measurements at high temperature using free-space methods," *IEEE Trans. Compon., Packag., Manuf. Technol.*, vol. 9, no. 6, pp. 1011–1019, Jun. 2019.
[28] J. W. Schultz, *Focused Beam Methods: Measuring Microwave Materials in Free Space*. New York, NY, USA: John Schultz, 2012.
[29] A. Mancini, J. L. Salazar, R. M. Lebron, and B. L. Cheong, "A novel technique to characterize the effect of rain over a radome for radar applications," in *Proc. IEEE Radar Conf. (RadarConf)*, May 2017, pp. 470–475.
[30] A. Mancini, J. L. Salazar, R. M. Lebrón, and B. L. Cheong, "A novel instrument for real-time measurement of attenuation of weather radar radome including its outer surface—Part II: Applications," *J. Atmos. Ocean. Technol.*, vol. 35, no. 5, pp. 975–991, May 2018.
[31] J. Dunsmore, "Gating effects in time domain transforms," in *Proc. 72nd ARFTG Microw. Meas. Symp.*, Dec. 2008, pp. 1–8.

ZEESHAN QAMAR (Member, IEEE) received the B.Sc. and M.Sc. degrees in electrical engineering from COMSATS University, Islamabad, Pakistan, in 2010 and 2013, respectively, and the Ph.D. degree in electronic engineering from the City University of Hong Kong, Hong Kong, in 2017. From July 2010 to August 2013, he was a Research Associate with the Department of Electrical and Computer Engineering, COMSATS University. From November 2017 to April 2018, he was a Postdoctoral Research Associate with the Department of Materials Science and Engineering, City University of Hong Kong. He is currently a Postdoctoral Research Fellow of the Phased Array Antenna Research and Development Group (PAARD) and the Advanced Radar Research Center (ARRC) with The University of Oklahoma, Norman, OK, USA. His current research interests include microwave/millimeter-wave circuits, material characterization, meta-materials, artificial dielectric layer, antennas and phased arrays, and phased array antennas. He is a member of the IEEE Antennas and Propagation Society (AP-S). He is also a Reviewer of various IEEE and IET conferences and journals.

NAFATI ABOSERWAL (Member, IEEE) received the B.S. degree in electrical engineering from Al-Mergheb University, Alkhoms, Libya, in 2002, and the M.S. and Ph.D. degrees in electrical engineering from Arizona State University, Tempe, AZ, USA, in 2012 and 2014, respectively. In January 2015, he joined the Advanced Radar Research Center (ARRC) and the Department of Electrical and Computer Engineering with The University of Oklahoma (OU), Norman, as a Postdoctoral Research Scientist. He is currently a Research Associate and the Manager of far-field, near-field, and environmental anechoic chambers with the Radar Innovations Laboratory (RIL). His research interests include EM theory, computational electromagnetics, antennas and diffraction theory, edge diffraction, and discontinuities impact on the array performance. His research also focuses on active high performance phased array antennas for weather radars, higher modes and surface waves characteristics of printed antennas, and high performance dual-polarized microstrip antenna elements with low cross-polarization. He is a member of the IEEE TRANSACTIONS ON ANTENNAS AND PROPAGATION.

JORGE L. SALAZAR-CERRENO (Senior Member, IEEE) received the B.S. degree in ECE from Antenor Orrego Private University, Trujillo, Peru, and the M.S. degree in ECE from the University of Puerto Rico at Mayagüez Campus (UPRM), in 2011, and the Ph.D. degree in ECE from the University of Massachusetts Amherst. His Ph.D. research was focused on the development of low-cost dual-polarized active phased array antennas (APAA). After graduation, he was awarded a prestigious Postdoctoral fellowship of the National Center for Atmospheric Research (NCAR) Advanced Study Program (ASP). At NCAR, he worked at the Earth Observing Laboratory (EOL) division developing airborne technology for two-dimensional, electronically scanned, and dual-pol phased array radars for atmospheric research. He joined the Advanced Radar Research Center (ARRC) with The University of Oklahoma, as a Research Scientist, in July 2014, and became an Assistant Professor with the School of Electrical and Computer Engineering, in August 2015. He is a Senior Member of the IEEE Antennas and Propagation Society (AP-S). His research interests include high-performance, broadband antennas for dual-polarized phased array radar applications, array antenna architecture for reconfigurable radar systems, APAA, Tx/Rx modules, radome EM modeling, and millimeter-wave antennas. In 2019, he was awarded the prestigious William H. Barkow Presidential Professorship from The University of Oklahoma for meeting the highest standards of excellence in scholarship and teaching. He is also a Reviewer of various IEEE and AMS conferences and journals.